UNIVERSITY OF OKLAHOMA

GRADUATE COLLEGE

EFFECT OF ALIGNMENT ON THERMAL CONDUCTIVITY ENHANCEMENT OF POLYETHYLENE/GRAPHENE NANOPLATELET COMPOSITE MATERIALS

A THESIS

SUBMITTED TO THE GRADUATE FACULTY

in partial fulfillment of the requirements for the

Degree of

MASTER OF SCIENCE

By

MORTAZA SAEIDI-JAVASH
Norman, Oklahoma
2017

EFFECT OF ALIGNMENT ON THERMAL CONDUCTIVITY ENHANCEMENT OF POLYETHYLENE/GRAPHENE NANOPLATELET COMPOSITE MATERIALS

A THESIS APPROVED FOR THE
SCHOOL OF AEROSPACE AND MECHANICAL ENGINEERING

BY

_____
Dr. Jivtesh Garg, Chair

_____
Dr. M. Cengiz Altan

_____
Dr. Feng C. Lai

I dedicate this thesis to my loving parents, **Karim Saeidi** and **Nahide Alipour** for their wonderful love, endless support, and encouragement during my life.

This work is also dedicated to my brother, **Reza Saeidi**, who has never left my side and has been greatly supportive. I love you all and I am so grateful for everything you have done and continue to do to make me who I am.

Acknowledgements

I am very fortunate to have performed my masters study at the University of Oklahoma; therefore, there are many people to thank for their part in my success. I would first like to thank my advisor, Dr. Jivtesh Garg, for his guidance and kindness throughout the course of this work. It could have never been accomplished without his tremendous support. I would also like to thank my thesis committee members, Professor M. Cengiz Altan, and Professor Feng C. Lai for their help and precious time. I am also thankful to Professor Brian Grady for his generosity and allowing me to access his laboratory and use DSC Micro-compounder. I would like to acknowledge and thank the School of Aerospace and Mechanical Engineering staff for their help and great support. Special thanks go to Billy Mays and Greg Williams for their kindness in providing me any assistance that I requested. I want to extend my special thanks to Professor Farrokh Mistree who is more than generous with his guidance and insightful advices.

I met so many great people during my studies at the University of Oklahoma that each person has had a significant impact on my graduate career that I will not forget. Finally, I am very much thankful to my family and all my friends for their continued support and encouragement.

Table of Contents

List of Tables

List of Figures

Abstract

Polymers offer several advantages such as low cost, light weight, corrosion resistance and ease of processing, however, they have much lower intrinsic thermal conductivity (<0.5 W/mK) compared to metals (> 20 W/mK) which hinders their widespread applicability in thermal management technologies. Enhancement in thermal conductivity of polymer materials will lead to their more widespread use in applications such as power electronics, electric motors and heat exchangers. The focus of this research is on the effect of molecular alignment on thermal conductivity enhancement of polyethylene/graphene (PE/GNP) nanoplatelet composite materials.

Pure high density polyethylene and PE/GNP nanocomposites with 7 and 10 wt% graphene nanoplatelets are prepared using melt-compounding method. Mechanical stretching is applied to achieve molecular chain alignment and several characterization techniques (Wide Angle X-ray Spectroscopy, Laser Scanning Confocal Microscopy, Scanning Electron Microscopy and Atomic Force Microscopy) are used to investigate the impact of mechanical stretching on PE chains and GNP flakes alignment. Finally, thermal conductivity of specimens is measured using a created set-up based on the Angstrom method. The obtained results demonstrate the promise of alignment effects in achieving high thermal conductivity values.

Chapter 1: Introduction

The use of carbon-based polymer nanocomposite materials has increased significantly over recent decades with applications ranging from aerospace structures to electronic packaging materials. They have great advantages in terms of weight, stiffness, durability, and the ability to form complex geometries. The thermo-electro-mechanical properties of polymers are improved by taking advantage of the superior performance of fillers, such as carbon fibers, carbon black, carbon nanotubes (CNTs), and graphene nanoplatelets (GNPs).

Polymer heat exchangers [1,2] (Figure 1.1) based on polymers such as polyethylene and polypropylene are widely used in applications including water desalination [3], solar energy harvesting [4], automotive control units [5] and micro-electronics cooling [6–8]. Polymers offer several advantages such as lower cost and weight which make them more economically competitive compared with metallic heat exchangers. Moreover, the energy required to produce polymers is about two times lower than common metals, making them environmentally attractive. Polymers, due to their resistance to chemicals, also improve reliability in corrosive environments such as natural gas liquefaction in offshore applications and condensing boilers where they hold potential to replace expensive metals such as titanium [9,10].

Polymeric materials have much lower intrinsic thermal conductivity (<0.5 W/mK) compared to metals (> 20 W/mK) which limits their more widespread applicability in thermal management technologies [11].

In this work polyethylene (PE) will be used as the base polymer and graphene nanoplatelets will be used as filler material due to their high intrinsic thermal conductivity (1500-5000 W/mK) [12–14]. Alignment has been explored as means to achieve high thermal conductivity. The structure of typical Polyethylene (PE) nanocomposites is shown in Figure 1.2. The polymer chains themselves exist in randomly oriented crystalline regions called lamellae which are interspersed with amorphous regions. While the thermal conductivity of the polymer within the crystalline regions is high, the random orientation of these leads to a convoluted heat conduction path which, leads to an overall poor thermal conductivity. Similarly, the GNPs are randomly oriented which also limits their contribution to thermal conductivity enhancement along a given direction. By aligning both the polymer lamellae and GNPs along a given direction (Figure 1.2), high thermal conductivity values along that direction can be achieved. Alignment in this work has been achieved by stretching. Stretching has been demonstrated to lead to alignment of both the polymer lamellae [15–17] and dispersed filler material [18–20]. This research uses simultaneous alignment for the first time to achieve nanocomposite with high thermal conductivity.

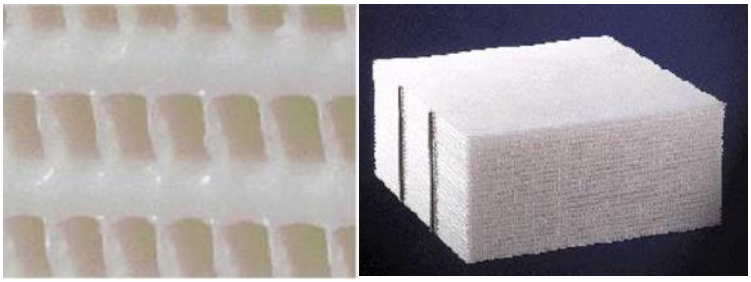

Figure 1.1. Monoblock polypropylene heat exchanger by AB Segerfrojd

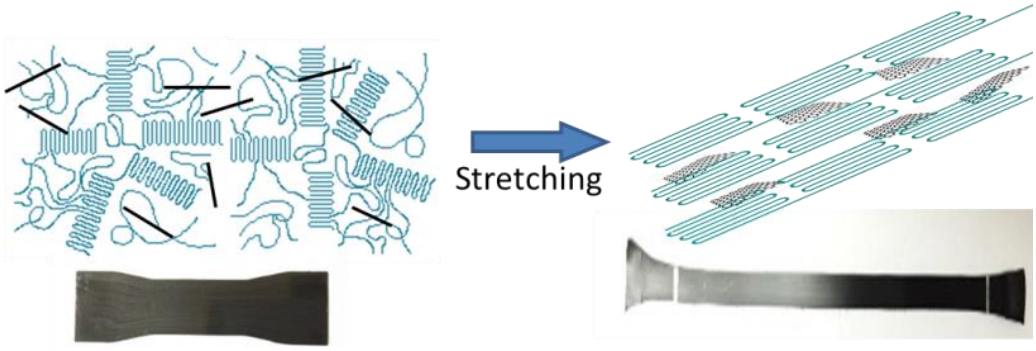

Figure 1.2. Highly aligned PE/GNP nanocomposite

Nysten *et al.* [21] studied both the longitudinal and the transverse thermal conductivity of a stretched polyethylene film with draw ratio of 40 to get a better understanding of the thermal conductivity in semi-crystalline polymers. They found that the alignment of the polymer chains can increase the longitudinal thermal conductivity to 10 W/mK at 100 K.

Henry *et al.* [22] used molecular dynamics simulations to calculate the thermal conductivity of single polyethylene chains. They estimated that the thermal conductivity of single PE chains can exceed 100 W/mK if the chain is longer than 40 nm. In another work Choy *et al.* [23] studied the thermal conductivity of oriented polyethylene both along and perpendicular to the draw direction for draw ratio between 1-25. They found that the thermal conductivity of the sample with draw ratio of 25 is 13.8 W/mK (at 300 K). Later the thermal conductivity of ultra-oriented polyethylene of ultrahigh molecular weight was measured 37.5 W/mK at draw ratio of 50 [24].

Recently, thermal conductivity of a single Polyethylene (PE) fiber with aligned chains (Figure 1.3) was measured to be 104 W/mK almost 200 times larger than thermal conductivity of bulk PE (~0.5 W/mK) [25]. Similarly in another work, PE films

comprised of highly aligned PE chains were found to exhibit thermal conductivity of almost 20 W/mK, comparable to thermal conductivity of metals such as titanium (~22 W/mK) [26].

Huang *et al.* [27] found that alignment of 0.4 vol% carbon nanotubes increase the thermal conductivity of carbon-based polymer nanocomposite to 0.65 W/mK. Aligned CNT arrays were fabricated using chemical vapor deposition (CVD) method. Marconnet *et al.* [28] recently demonstrated alignment of carbon-nanotubes in a polymer matrix to result in a composite *k* of ~ 4.8 W/mK (almost 20 times higher than the base polymer). In this study only the dispersed CNTs were aligned but not the base polymer.

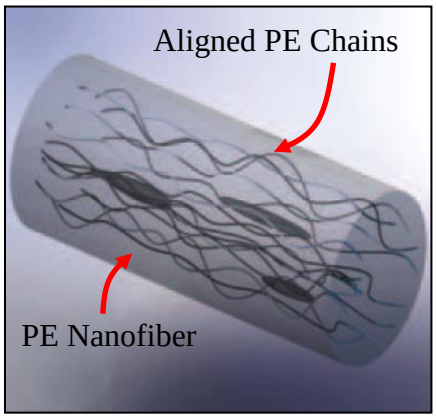

Figure 1.3. Polyethylene fiber with aligned chains [25]

1.1 Objective of this Thesis

The objective of this thesis work is to study the impact of simultaneous alignment of polymer chains and graphene nanoplatelets on the thermal conductivity of polyethylene/graphene nanocomposites. Above large enhancements in thermal conductivity through alignment of either the base polymer or the dispersed nano-filler suggests that even higher enhancement in thermal conductivity values can be achieved if

both the polymer matrix and the dispersed nanofiller (GNPs in this work) are simultaneously aligned. Extensive experimental work has been done for the first time to support this hypothesis.

Chapter 2: Polymer Nanocomposite Synthesis

In this chapter materials and methods implemented for polyethylene/graphene (PE/GNP) nanoplatelet composite material synthesis have been explained. High density polyethylene is used as a matrix and graphene nanoplatelets (~ 60 nm thickness and ~ 5 μm lateral size) are as a filler for nanocomposite fabrication. Polymer nanocomposites are prepared using melt-compounding.

2.1 Materials

2.1.1 High Density Polyethylene

The polyethylene used in this study was high density polyethylene with melt index 2.2 g/10 min available from Sigma-Aldrich. The properties of this polymer are shown in Table 2.1.

Table 2.1. High density polyethylene properties (from Sigma-Aldrich)

Melt index	2.2 g/10 min (190 °C/2.16kg)
Hardness	65 (Shore D, ASTM D 2240)
Transition temperature	Softening point 123 °C (Vicat, ASTM D 1525)
Density	0.93-0.97 (g/cm3)
Linear formula	$H(CH2CH2)_nH$

High density polyethylene has been chosen as a matrix for in this study because it already possesses a high thermal conductivity value in comparison to other polymers [29–32]. Moreover, the effect of polyethylene chains alignment on thermal conductivity enhancement has been well studied [21–25].

2.1.2 Specific Heat and Density Measurement of High Density Polyethylene

Specific heat of the pure high density polyethylene specimen is measured using Differential Scanning Calorimetry (DSC) technique. Moreover, density of high density polyethylene is measured using Pycnometer (AccuPyc 1340V2.0). Tables 2.2 and 2.3 present the specific heat analysis and density of pure polyethylene respectively.

Table 2.2. Specific heat analysis of high density PE

Temperature (ºC)	Specific Heat (J/gºC)
0	2.0
6.85	2.0
16.85	2.1
26.85	2.1
36.85	2.2
46.85	2.4
56.85	2.5

Table 2.3. Density measurement of PE

Density of PE (g/cm^3)	0.98

2.1.3 Graphene

Graphene is a two-dimensional (2D) material, formed of a lattice of hexagonally arranged carbon atoms. The term graphene is typically applied to a single layer of graphite, although common references also exist to bilayer or trilayer graphene. Most thermal properties of graphene are derived from those of graphite and bear the imprint of the highly anisotropic nature of this crystal. For instance, the in-plane covalent sp^2 bonds between adjacent carbon atoms are among the strongest in nature (slightly stronger than

the sp^3 bonds in diamond), with a bonding energy of approximately 5.9 eV. By contrast, the adjacent graphene planes within a graphite crystal are linked by weak van der Waals interactions (~ 50 meV) with a spacing of h ≈ 3.35 Å. The strong and anisotropic bonding and the low mass of the carbon atoms give graphene and related materials unique thermal properties [33].

Fugallo *et al.* [12] using first-principles transport calculations found that at room temperature, the highest predicted thermal conductivity has the value of 3600 W/mK for naturally occurring graphene and 4300 W/mK for the isotopically pure graphene. In another study, Balandin *et al.* [13] experimentally demonstrated 2D to 3D dimensional crossover of heat conduction in few layer graphene (FLG). They prepared FLG samples by standard mechanical exfoliation of bulk graphite and suspended across trenches in Si/SiO_2. The width of the suspended flakes was 5 to 16 μm. They extracted thermal conductivity values in the range of 3080-5150 W/mK for a set of graphene flakes.

Recently, Balandin [34] demonstrated that in-plane thermal conductivity of graphene at room temperature is among the highest of any known material, about 2000–4000 W/mK for freely suspended samples. The upper end of this range is achieved for isotopically purified samples with large grains, [35] whereas the lower end corresponds to isotopically mixed samples or those with smaller grain sizes. Naturally, any additional disorder or even residue from sample fabrication [36] will introduce more phonon scattering and lower these values further. For comparison, the thermal conductivity of natural diamond is ~2200 W/mK at room temperature [37,38] (that of isotopically purified diamond is 50% higher, or ~ 3300 W/mK). In particular, Figure 2.1 shows

presently known ranges of thermal conductivity at room temperature, with the implication that all lower bounds could be further reduced in more disordered samples.

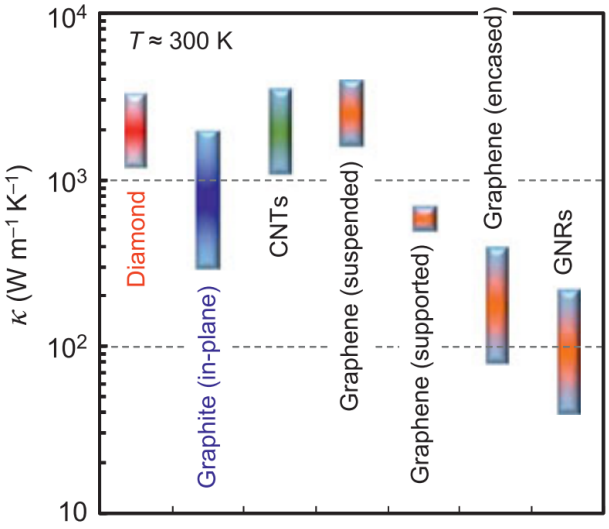

Figure 2.1. Room-temperature ranges of thermal conductivity k for diamond, graphite (in plane), carbon nanotubes (CNTs), suspended graphene, SiO_2-supported graphene, SiO_2-encased graphene, and GNRs [33]

By contrast, heat flow in the cross-plane direction of graphene and graphite is strongly limited by weak interplane van der Waals interactions. The thermal conductivity along the cross-plane direction of pyrolytic graphite is a mere ~ 6 W/mK at room temperature [39].

2.1.4 Characterization of Graphene Flakes

2.1.4.1 Size and Thickness Measurement of GNP Flakes Using Scanning Electron Microscopy (SEM) and Atomic Force Microscopy (AFM)

Highest quality graphene with minimal defect density has been used for this study to facilitate achievement of ultra-high thermal conductivities. The flakes used in this study have very low defect density due to being produced directly from raw graphite by

mechanical exfoliation. Table 2.4 presents the properties of graphene flakes used in this study.

Table 2.4. Specifications of GNP flakes available at Graphene Supermarket

Average flake thickness	~ 60 nm
Specific surface area	<15 m^2/g
Color	Black
Purity	98.5%
Particle (lateral) size	~ 3-7 microns

The thickness of GNP flakes has been characterized using an Asylum Research MFP-3D atomic force microscope (AFM) in the tapping mode (Figure 2.2). The lateral size of the GNP flakes has been measured through scanning electron microscopy (SEM) using a Zeiss NEON 40EsB High resolution SEM. Figure 2.3 shows the SEM images of graphene flakes indicating roughly 5 μm large flakes interspersed with some larger flakes.

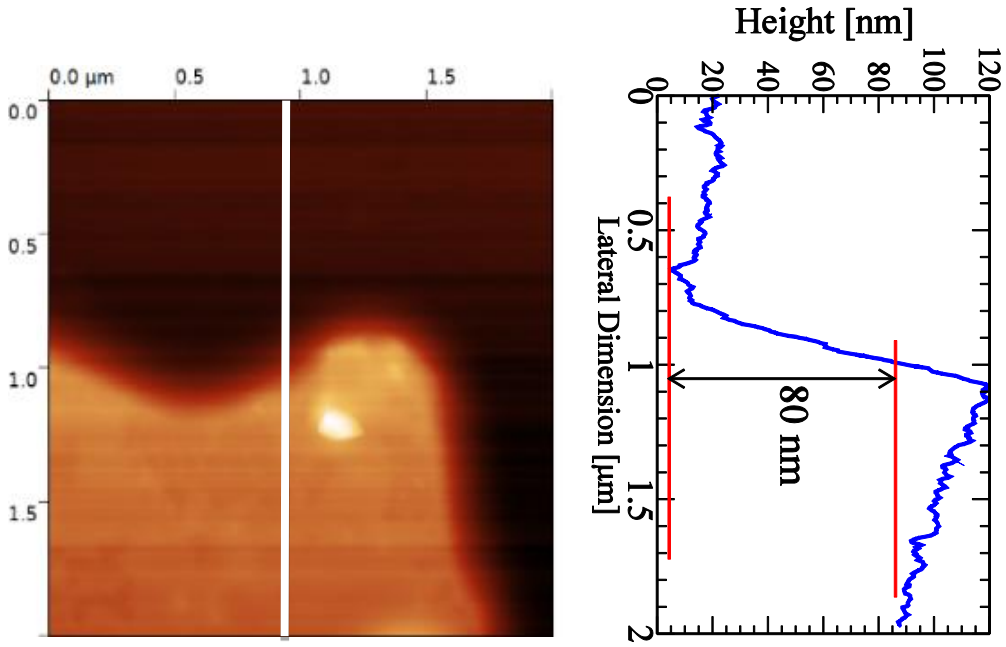

Figure 2.2. AFM image of a GNP flake showing an ~80 nm thick flake

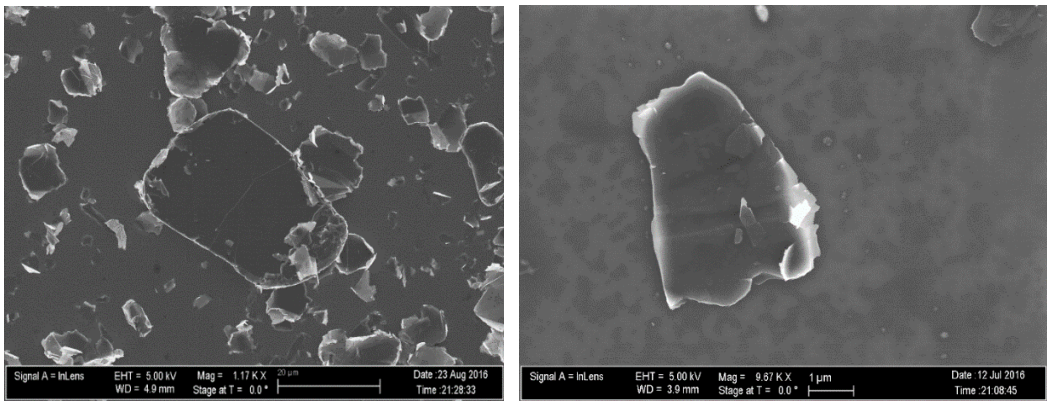

Figure 2.3. SEM images of GNP flakes for lateral size characterization

2.1.4.2 Raman and X-ray Photoelectron Spectroscopy of Graphene

Raman spectroscopy (and Raman imaging) has become a powerful, noninvasive method to characterize graphene and related materials. A large amount of information such as disorder, edge and grain boundaries, thickness, doping, strain and thermal conductivity of graphene can be learned from the Raman spectrum and its behavior under

varying physical conditions. Raman spectroscopy uses a monochromatic laser to interact with molecular vibrational modes and phonons in a sample, shifting the laser energy down (Stokes) or up (anti-Stokes) through inelastic scattering. Identifying vibrational modes using only laser excitation, Raman spectroscopy has become a powerful, noninvasive method to characterize graphene and related materials [40].

In graphene, the Stokes phonon energy shift caused by laser excitation creates two main peaks in the Raman spectrum: G (1580 cm^{-1}), a primary in-plane vibrational mode, and 2D (2690 cm^{-1}), a second-order overtone of a different in-plane vibration, D (1350 cm^{-1}). The G band position is highly sensitive to the number of layers present in the sample and is one method for determining layer thickness and is based upon the observed position of this band for a particular sample. The D band is known as the disorder band or the defect band and it represents a ring breathing mode from sp^2 carbon rings, although to be active the ring must be adjacent to a graphene edge or a defect. The band is typically very weak in graphite and is typically weak in high quality graphene as well. If the D band is significant it means that there are a lot of defects in the material.

The intensity of the D band is directly proportional to the level of defects in the sample. The last thing to note about the D band is that it is a resonant band that exhibits what is known as dispersive behavior. This means that there are a number of very weak modes underlying this band and depending on which excitation laser is used, different modes will be enhanced. The consequence of this is that both the position and the shape of the band can vary significantly with different excitation laser frequencies, so it is important to use the same excitation laser frequency for all measurements when characterizing with the D band. The 2D band is the second order of the D band, sometimes

referred to as an overtone of the D band. It is the result of a two-phonon lattice vibrational process, but unlike the D band, it does not need to be activated by proximity to a defect. As a result, the 2D band is always a strong band in graphene even when there is no D band present, and it does not represent defects. This band is also used to determine graphene layer thickness.

Raman spectra in this work were collected using a Horiba LabRam HR Raman confocal microscope with a 633 nm laser, 300 grooves/mm grating, 50 micron pinhole, and 50x objective lens.

Oxygen content of graphene is also measured through X-ray photoelectron spectroscopy (XPS) using an Omicron XPS system with a DAR400 dual Mg/Al X-ray source and an Argus detector. Figure 2.5 shows the XPS analysis of Sample-C graphene indicating an oxygen content of only 2.8%.

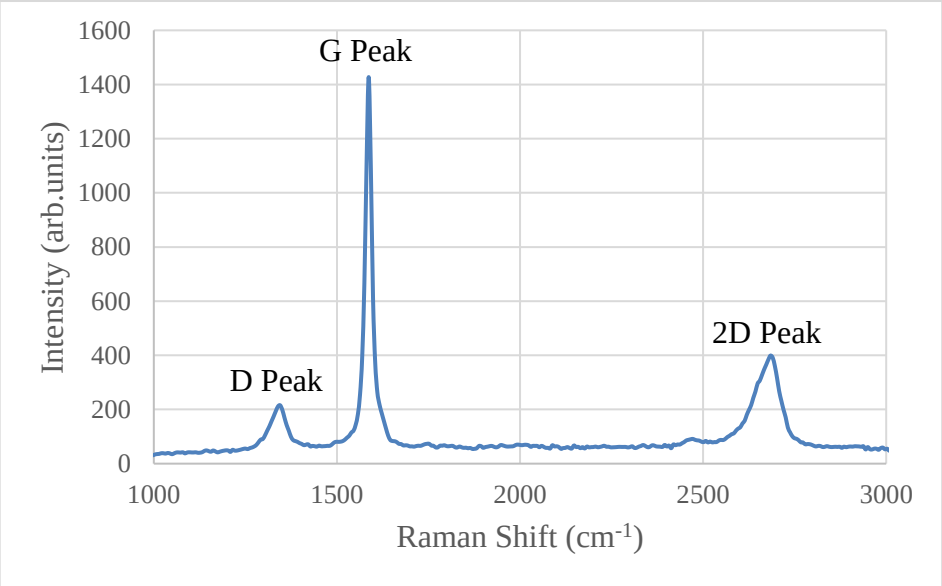

Figure 2.4. Raman spectra for GNP

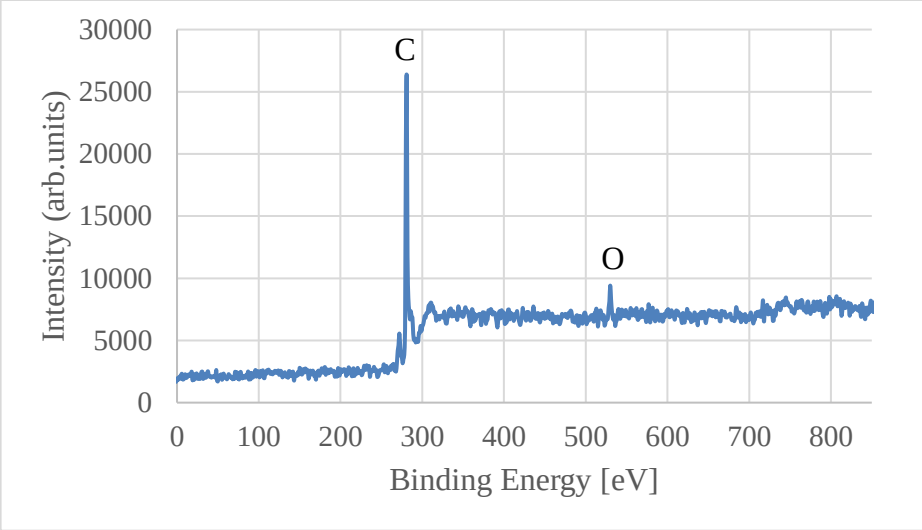

Figure 2.5. XPS analysis of the graphene

2.2 Processes Involved

2.2.1 Micro-compounding

DSM Xplore 5 cc micro-compounder (Figure 2.6) has been used for PE/GNP nanocomposite fabrication by melting and mixing polyethylene pellets and graphene nanoplatelets. In melt-compounding a mixture of polymer pellets and filler material is melted and mixed for a pre-determined time under high shear conditions in a sealed mixing compartment containing two conical mixing screws.

Figure 2.6. DSM Xplore 5 cc micro-compounder

Two key variables that determine the uniformity of dispersion of graphene within the nanocomposite are the mixing time and mixing temperature. Mixing times ranging from 4 min to 90 mins and mixing temperatures of 180 °C to 270 °C has been used during the study. Increasing the mixing time provides a more uniform dispersion; longer times however can also damage the GNPs. Furthermore, lower temperature prevents to achieve a well-dispersed graphene flakes and also higher temperature damages the polyethylene chains. It has been observed that 200-220 ºC is the optimal temperature for compounding polymer nanocomposites.

2.2.2 Compression Molding

At the end of mixing period as the mixture of melted polyethylene and GNPs is taken out, the blended material is compression-molded using 1 MPa pressure at 145 C for 15 min to fabricate approximately 1-mm-thick specimens for stretching. The pressure was sustained while the specimens were allowed to cool down gradually to the ambient temperature (typically, 23 C) at a typical rate of 2.5 C/min. Carver hot press has been used for molding.

Figure 2.7. Carver hot press for compression molding

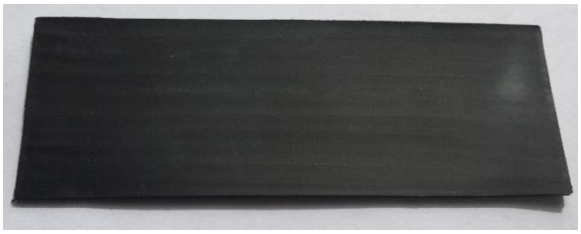

Figure 2.8. PE/GNP sample before stretching

2.2.3 Mechanical Stretching

Alignment of PE chains and GNPs within the nanocomposite has been achieved by mechanical stretching. We used a motor driven apparatus, capable of applying 100 lb of force, to stretch the nanocomposites (Figure 2.9). The slide can apply very low strain rates of 20μm/min which is desirable to ensure uniform stretching and prevent sample failure. Brittle failure of the samples is also overcome by heating the sample to 60-70 °C by using a heater. The heater itself is placed on another motorized platform to move it back and forth along the length of the sample to ensure uniform stretching.

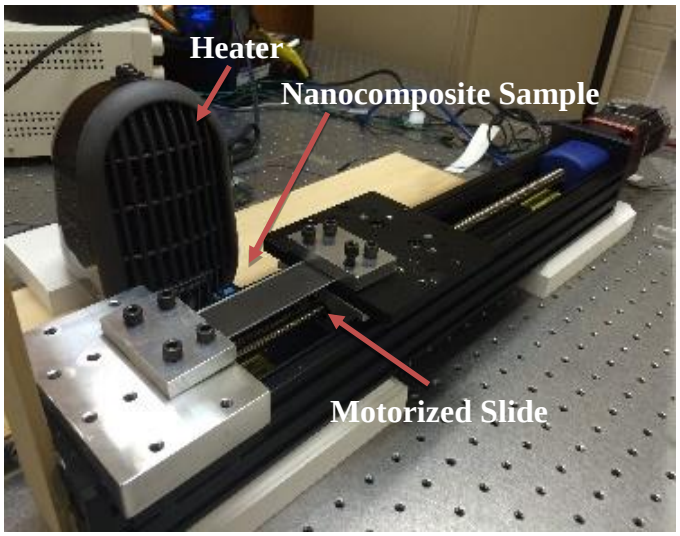

Figure 2.9. Linear motorized slide used for mechanical stretching

Using this set-up we were able to achieve high stretch ratios. Figure 2.10 shows a stretched sample with draw ratio of 5.

Figure 2.10. Stretched PE/GNP specimen with draw ratio of 5

Chapter 3: Thermal Conductivity Measurement

This chapter describes thermal conductivity measurement of the polyethylene-graphene nanocomposite samples. Thermal conductivity is measured through the measurement of thermal diffusivity (K), specific heat (s) and density (ρ) using the relationship, $k = \rho s K$. Specific heat is measured using a differential scanning calorimeter while density is measured using the Archimedes principle. Thermal diffusivity in this work is measured using the Angstrom method described below.

3.1 Angstrom Method

Through the Angstrom method thermal diffusivity is measured by measuring the diffusion of heat along a material by applying a periodic heat pulse at one end while the other end is left at the temperature of the surrounding medium. A heat wave propagates down the length of the material, both losing amplitude and experiencing a phase shift. The fluctuations in temperature as a function of time are measured at two locations along the sample, comparison of the temperature waves leads to a determination of the thermal diffusivity value for the material.

Considering that the temperature changes in this experiment are periodic, the measurements of the power input used to heat the system are not required. Also, instead of absolute measurements of the temperature, only relative changes in magnitude of temperature as a function of time and position must be recorded. For this experiment applied periodic heat pulse at one end of the sample will cause a temperature pulse to travel down the length of the sample. Part of the heat traveling down the length of the sample will be transmitted through conduction, part will heat the sample itself, and part

of the heat will be lost to the air through radiation. The heat transfer equation in the sample can be written as

$$\underbrace{\iiint \frac{dQ}{dt} dV}_{\text{Created in Rod}} - \underbrace{\oiint R(T-T_0)ds}_{\textit{Lost}\text{ to radiation}} + \underbrace{\oiint k\bar{\nabla}T.ds}_{\text{Heat conducted}} = \underbrace{\iiint s\rho \frac{\partial T}{\partial t} dV}_{\text{Change in rod's temperature}} \tag{3.1}$$

where *T* is the temperature, ∇ is the gradient operator, *ds* is an element of surface area, and *k* is the thermal conductivity of the rod. Because there is no heat source within the rod, equation 1 can be simplified using $\frac{dQ}{dt} = 0$ Green's first theorem is used to transform the integral over the surface in the second and third term on left side of eq. (3.1) into a volume integral. For a rod of cross sectional area, *A* and perimeter *P*, the above heat transfer equation is transformed into:

$$k\frac{\partial^2 T}{\partial x^2} - s\rho\frac{\partial T}{\partial t} - \frac{PR}{A}(T-T_0) = 0 \tag{3.2}$$

where T is the temperature, T_0 is the ambient temperature and R represents the emissivity of the material. T_0 further simplify the equation, we can replace T-T_0 and rewrite it as $\theta \equiv T - T_0$

In this experiment, a periodic heat wave with a frequency of $w = 2\pi f$ (*f* is the inverse of the period of the heat wave) is applied to the rod. The solution for the temperature profile can be written as a sum over all the harmonics as,

$$\theta(x,t) = \sum_{n=-\infty}^{\infty} C_n(x)e^{inwt} \tag{3.3}$$

Substituting eq. (3.3) into eq. (3.2), leads to the following equation for $C_n(x)$ (eq. 3.4)

$$\sum (K\frac{\partial^2 C_n}{\partial x^2} - HC_n - inwC_n)e^{inwt} = 0 \tag{3.4}$$

where $K = \frac{k}{s\rho}$, $H = \frac{PR}{As\rho}$,. Because of a complete orthogonal set in eq. (3.4), all coefficients must disappear. Then:

$$K\frac{\partial^2 C_n}{\partial x^2} - C_n(H + inw) = 0 \tag{3.5}$$

The solution of eq. (3.5) is:

$$C_n(x) = C_{n0}e^{\pm\sqrt{\lambda_n}x} \tag{3.6}$$

Where $\lambda_n = \frac{H + inw}{K}$ and $\sqrt{\lambda_n} = \alpha_n + i\beta_n$. Then $\lambda_n = (\alpha_n + i\beta_n)^2 = \alpha_n^2 + 2i\alpha_n\beta_n - \beta_n^2$

By setting the real and imaginary parts of λ_n equal to each other, we get eqs. (3.7) and (3.8);

$$\alpha_n^2 - \beta_n^2 = \frac{H}{K} \tag{3.7}$$

$$2\alpha_n\beta_n = \frac{nw}{K} \tag{3.8}$$

Thermal diffusivity is determined through the knowledge of α_n and β_n which are determined experimentally using the method described below. By plugging the eq. (3.6) into eq. (3.3), we get

$$\theta(x,t) = \sum_{n=-\infty}^{\infty} C_{n0}e^{\pm\sqrt{\lambda_n}x}e^{inwt} \tag{3.9}$$

Since the temperature decays with increasing length, the chosen solution of eq. (3.9) is,

$$\theta(x,t) = \sum_{n=-\infty}^{\infty} C_{n0}[e^{-\sqrt{\lambda_n}x}][e^{inwt}] \tag{3.10}$$

Plugging $\sqrt{\lambda_n} = \alpha_n + i\beta_n$ in eq. (3.10) leads to

$$\theta(x,t) = \sum C_{n0} e^{-\alpha_n x} e^{i(nwt-\beta_n x)} \tag{3.11}$$

The coefficient C_{n0} determine the form of the heat wave at $x=0$. As a general solution, assume $C_{n0} = A_{n0} e^{i\gamma}$, where A_{n0} and γ_n are real numbers. One of the particular solutions of the eq. (3.11) is:

$$\theta(x,t) = \sum A_{n0} e^{-\alpha_n x} \sin(nwt - \beta_n x + \gamma_n) \tag{3.12}$$

For the temperature variation, the imaginary part of the complex function has been chosen. In this experiment, temperature variation with respect to time at two different points along the sample, x_1 and x_2 is measured and recorded (see Figure 3.1).

The amplitude of the nth sine wave at x_1 is A_{n1} and can be represented by $A_{n1} = A_{n0} e^{-\alpha_n x_1}$; the corresponding phase constant is $\phi_{n1} = -\gamma_n - \beta_n x_1$. At x_2 the amplitude for the same harmonic is $A_{n2} = A_{n0} e^{-\alpha_n x_2}$ and the related phase constant is $\phi_{n2} = -\gamma_n - \beta_n x_2$ The ratio of the amplitude is

$$r_n = \frac{A_{n1}}{A_{n2}} = \frac{A_{n0} e^{-\alpha_n x_1}}{A_{n0} e^{-\alpha_n x_2}} = e^{-\alpha_n (x_1 - x_2)} \tag{3.13}$$

From the above equation α_n can be determined through the measurement of amplitude ratio and the distance between the thermocouples using the following equation,

$$\alpha_n = \frac{\ln r_n}{(x_2 - x_1)} \tag{3.14}$$

where $L = (x_2 - x_1)$ is the distance between two temperature locations as shown in Figure 3.1. The difference in phase of the two harmonics at the points x_1 and x_2 is

$$\phi_{n12} = \phi_{n1} - \phi_{n2} = (-\gamma_n - \beta_n x_1) - (-\gamma_n - \beta_n x_2) = \beta_n (x_2 - x_1) \tag{3.15}$$

From the above equation β_n can be determined through the measurement of phase difference and the distance between the thermocouples using the following equation,

$$\beta_n = \frac{\phi_{n12}}{(x_2 - x_1)} \tag{3.16}$$

By plugging eqs. (3.14) and (3.16) into eq. (3.8) for the first harmonic we obtain,

$$K = \frac{k}{s\rho} = \frac{wL^2}{2\phi_{n12}(\ln \frac{A_{n1}}{A_{n2}})} \tag{3.17}$$

Where K is the thermal diffusivity and k represents thermal conductivity. Since $\Delta t = \frac{\phi_{n12}}{w}$ thermal diffusivity can be derived using

$$K = \frac{\Delta x^2}{2\Delta t(\ln \frac{A_1}{A_2})} \tag{3.18}$$

where Δt is time delay of the sine wave between thermocouple 1 and 2. Therefore, when one end of the sample was heated by sine periodic heat wave and other end just placed in ambient temperature, measurement of the phase difference and amplitude ratio of the two temperature profiles (as shown in Figure 3.1) yields the thermal diffusivity.

3.2 Sample Preparation for In-plane Thermal Conductivity Measurement

Preparing samples for in-plane thermal conductivity measurement using the Angstrom method includes creating a small resistance heater with 1-2 mm width in the middle of specimens (Figure 3.1). A high resistance wire with resistance of 80 Ω/ft is used for making the heater and it is covered with high thermal conductivity thermal paste to create a perfect contact with the sample. After making the heater, two thermocouples are attached to the sample with 2 and 6 mm distance from the heater respectively. A

sinusoidal heat wave has been applied through the heater using a function generator and temperature profile at both locations are detected using a data acquisition system.

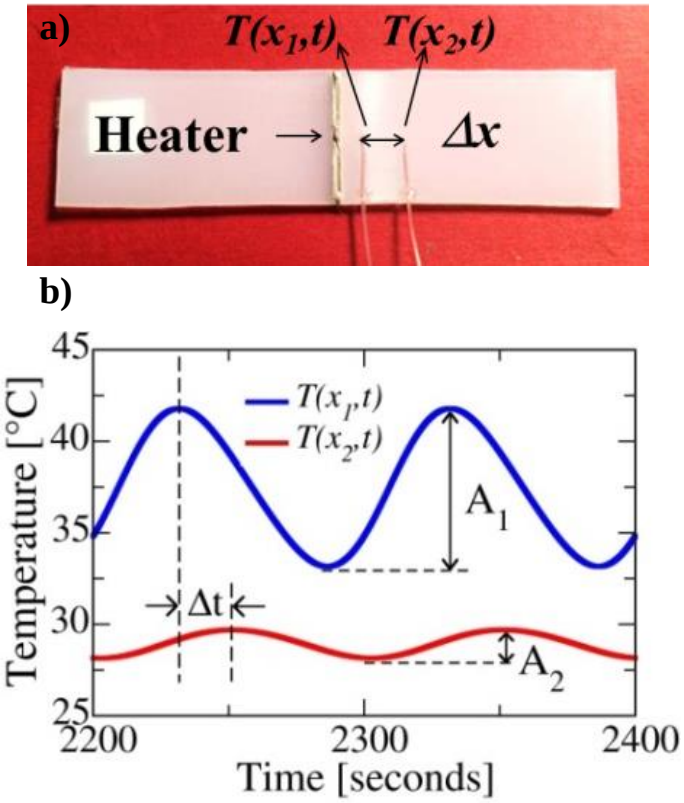

Figure 3.1. Thermal diffusivity measurement using Angstrom method, a) prepared sample, b) temperature profiles

Figures 3.2 and 3.3 show the extracted temperature profiles for PE/GNP with 7 and 10 wt% graphene at draw ratio 4.

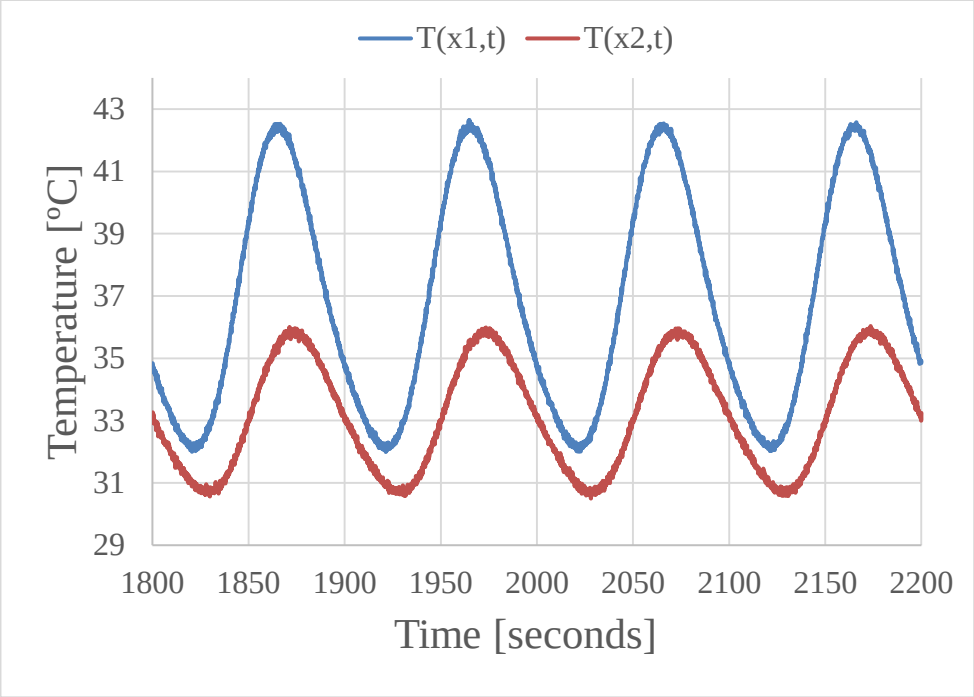

Figure 3.2. Temperature profiles for PE/GNP (7 wt%) at draw ratio 4

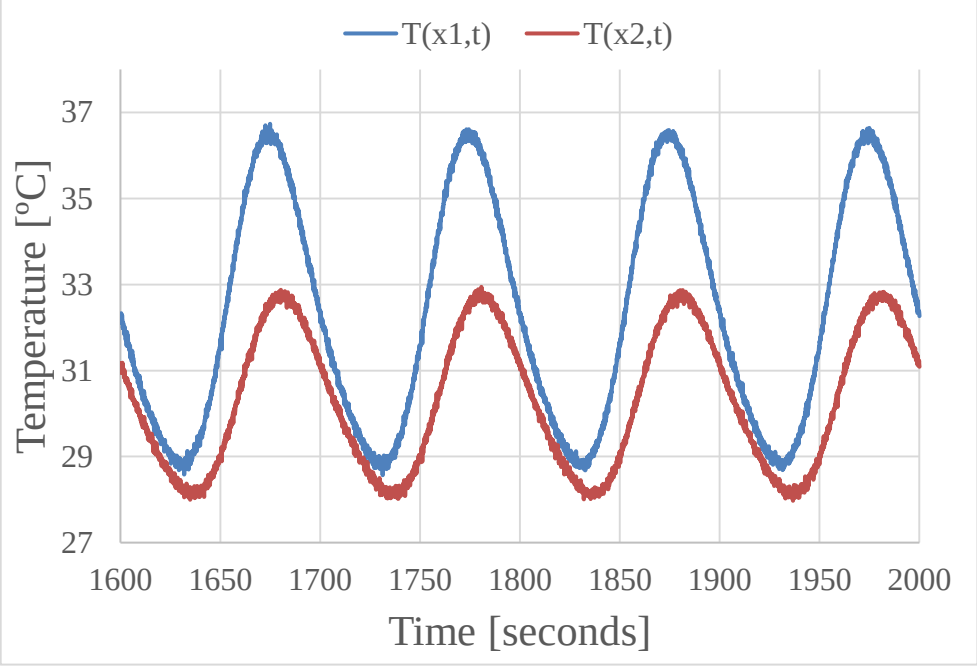

Figure 3.3. Temperature profiles for PE/GNP (10 wt%) at draw ratio 4

The in-plane thermal diffusivity measurement is performed inside a high vacuum chamber. The chamber is evacuated to below 15 mTorr using a turbo pump in order to eliminate the convection heat loss effect. Figure 3.2 shows the created set-up.

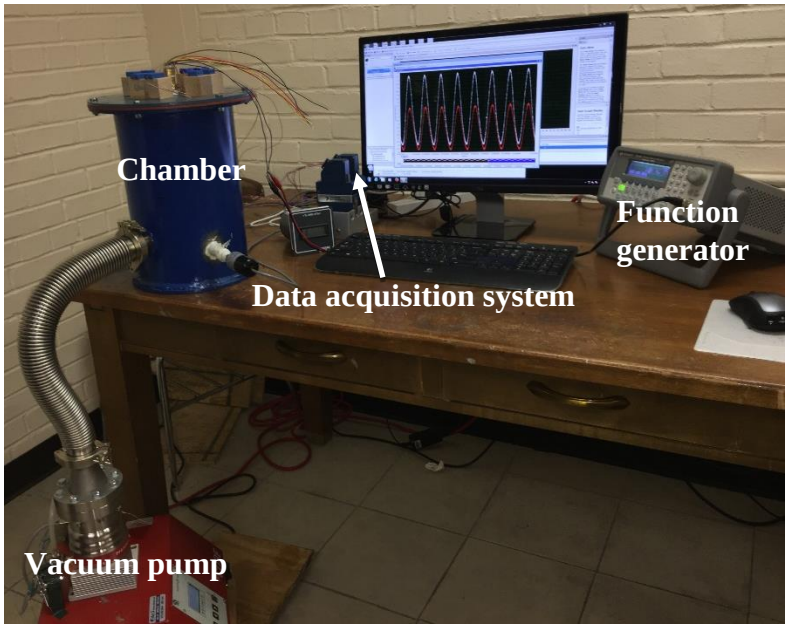

Figure 3.4. Thermal diffusivity measurement set-up based on the Angstrom method

Thermal conductivity has been calculated using the follow equation:

$$k = \rho s K \tag{3.19}$$

Where k is thermal conductivity, K is thermal diffusivity, ρ is density and s is specific heat. Specific heat and density are measured using Pycnometer (AccuPyc 1340V2.0) and Differential Scanning Calorimeter (DSC-Q1000) respectively.

3.3 Validation of the Angstrom Method by Comparison with Experiment

In order to validate the accuracy of the Angstrom method for in-plane thermal conductivity measurement, a comparison between thermal conductivity of unstretched pure polyethylene measured using the Angstrom method and reported values in the

literature has been conducted. According to the literature [30,32], thermal conductivity of pure PE is 0.4-0.5 W/mK. Using the Angstrom method, we were able to achieve 0.5 W/mK for thermal conductivity of pure PE. It revealed that the Angstrom method is significantly accurate and very reliable for this study. Moreover, the Angstrom method is benchmarked with Laser Flash Method (LFA) and a good agreement between the two methods was obtained.

3.4 Error Analysis of Thermal Diffusivity Measurement

Error analysis was performed to calculate the inaccuracy in thermal diffusivity measurement using the Angstrom method.

The main error source in thermal diffusivity measurement using the Angstrom method is the distance between the attached thermocouples to the specimen. We observed that the distance between thermocouples can vary up to $0.3\,mm$. This leads to $15\,\%$ error in thermal diffusivity measurement.

As aforementioned thermal diffusivity is measured using the below equation:

$$K = \frac{\Delta x^2}{2\Delta t(\ln \frac{A_1}{A_2})} \tag{3.20}$$

And since the main error is caused from the distance between thermocouples then;

$$dK = \frac{2\Delta x d(\Delta x)}{2\Delta t(\ln \frac{A_1}{A_2})} \tag{3.21}$$

From eq. (3.21) we could extract

$$\Delta K = \frac{2\Delta x}{2\Delta t(\ln \frac{A_1}{A_2})} d(\Delta x) \tag{3.22}$$

based on eq. (3.22) we have;

$$\frac{\Delta K}{K} = \frac{2d(\Delta x)}{\Delta x} = \frac{2(0.3)}{4} = 15\%$$

Using this analysis, the error bars are included in the results presented in chapter 5.

Chapter 4: Characterization of Alignment

This chapter describes the techniques used for characterization of alignment of both the polyethylene chains and dispersed graphene flakes. Scanning Electron Microscopy (SEM) and Wide Angle X-ray Spectroscopy (WAXS) are used for characterization of alignment of polyethylene chains and Laser Scanning Confocal Microscopy (LSCM) is implemented for characterization of alignment of graphene flakes.

4.1 Characterization of Alignment of Polyethylene Chains Using Scanning Electron Microscopy (SEM)

SEM is currently the most popular of the microscopic techniques, due to the user-friendliness of the apparatus, the ease of specimen preparation, and the general simplicity of image interpretation. The obvious limitation is that only surface features are easily accessible. In a SEM, a focused electron beam (energies between 1 and 50 keV) scans line by line over the specimen surface in the evacuated microscope column and forms signals based on the interactions between the beam and the sample, which are electronically detected and amplified.

Scanning electron microscopy using a Zeiss NEON 40EsB High resolution SEM was performed for characterization of alignment of pure polyethylene sample. As seen in Figure 4.1, polyethylene chains are oriented along the stretch direction.

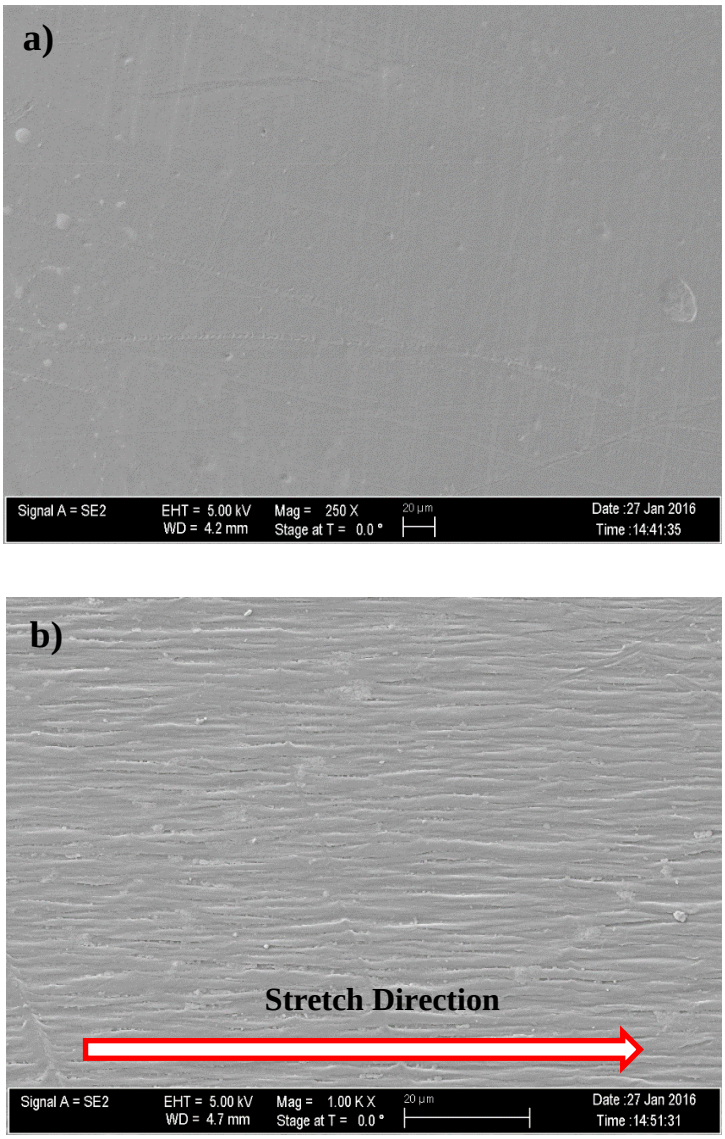

Figure 4.1. SEM images of pure polyethylene, a) Unstretched sample, b) Stretched PE with draw ratio of 5 along the longitudinal direction

The alignment of PE chains is also shown in Figure 4.2, comparing the unstretched and stretched PE with draw ratio of 5, at a very high magnification (10K).

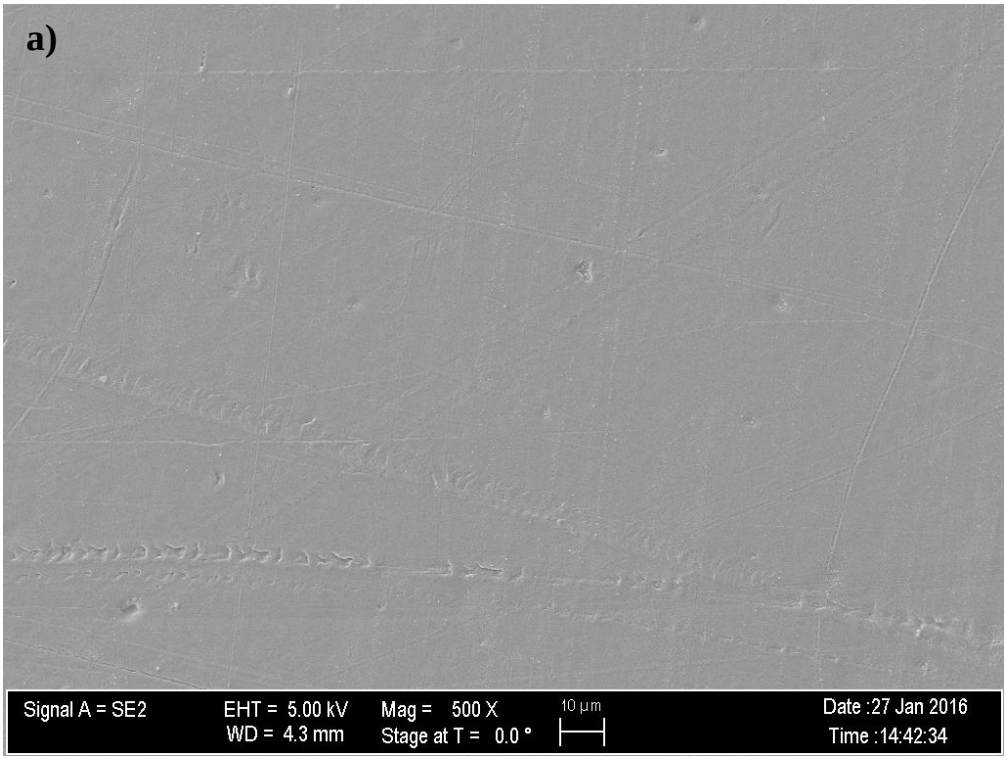

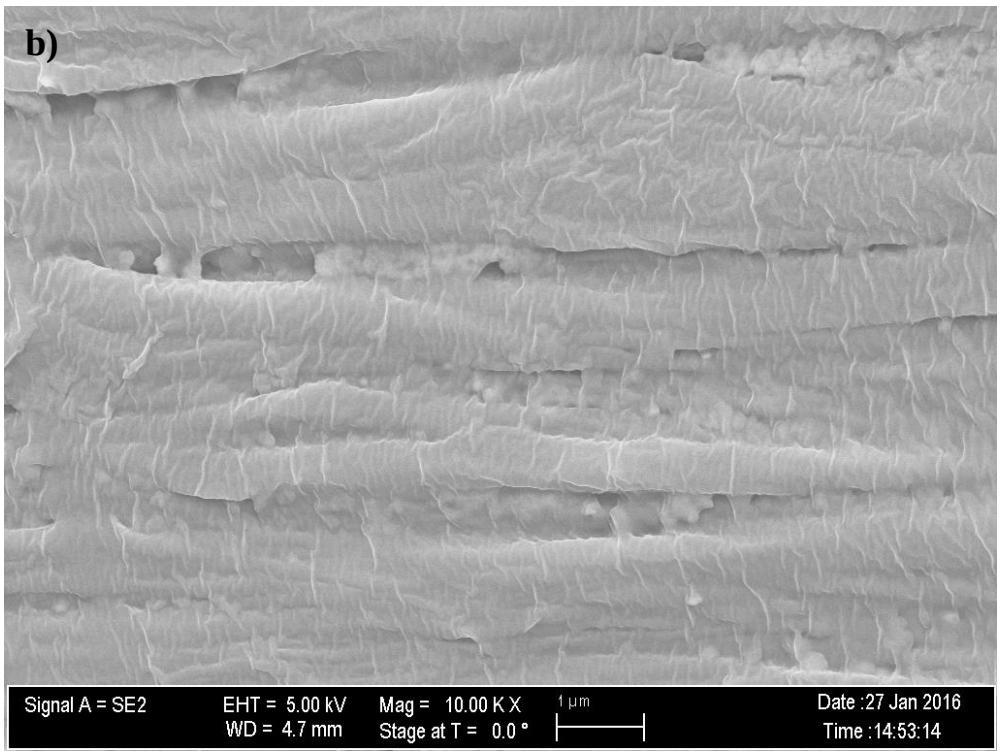

Figure 4.2. High magnification SEM images of pure polyethylene, a) Unstretched sample b) Stretched PE with draw ratio of 5 along the longitudinal direction

4.2 Characterization of Alignment of Polyethylene Chains Using Wide Angle X-Ray Scattering (WAXS) Spectroscopy

The undrawn polyethylene sample has randomly oriented stacks of crystallites. Upon drawing, the stacks begin to arrange in the drawing direction and beyond the yield point, the stacks begin to transform into fiber-like entities. These fibrous structures are composed of piled lamellae with long range order and/or tightly packed extended chains which are highly oriented in the drawing direction. As the fibrous structures are formed by the orientation process, significant changes in the patterns of both wide and small angle X-ray scattering (WAXS and SAXS) experiments are evident.

Wide-angle X-ray Scattering (WAXS) or wide-angle X-ray Diffraction (WAXD) is an X-ray-diffraction technique that is often used to determine the crystalline structure of polymers. This technique specifically refers to the analysis of Bragg peaks scattered to wide angles, which (by Bragg's law) implies that they are caused by sub-nanometer-sized structures. Orientation was measured as a function of draw ratio by wide-angle X-ray scattering. Each sample required data acquisition at two different scattering angles (2θ).

The WAXS measurements were obtained using the coordinate system defined in Figure 4.3. The Z axis is defined as the crystalline chain axis (the c-axis) and the angles α, β and ε are the angles between the stretching direction, **S**, and the X, Y, and Z axes, respectively. In Figure 4.3, the points a, b and c from a crystalline reflection plane that has a unit vector, N, normal to the plane surface. The angle of orientation (ϕ) is the angle between **N** and a unit vector, **S**, in the stretching direction.

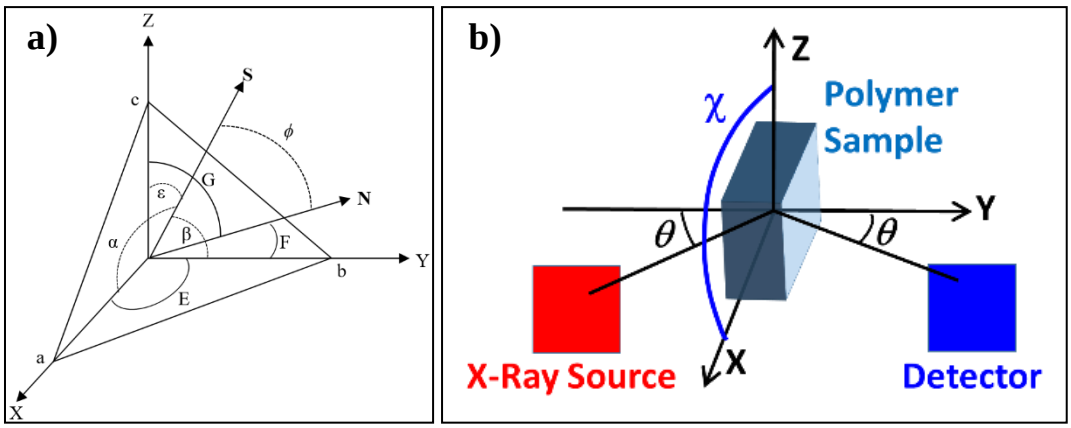

Figure 4.3. Orientation of polymer chains with respect to stretch direction a) WAXS coordinate system, b) WAXS experimental geometry

$$S = \cos(\alpha)\vec{i} + \cos(\beta)\vec{j} + \cos(\varepsilon)\vec{k} \tag{4.1}$$

$$N = \cos(E)\vec{i} + \cos(F)\vec{j} + \cos(G)\vec{k}$$
$$N = e\vec{i} + f\vec{j} + g\vec{k} \tag{4.2}$$

The coefficients of **N** are denoted *e*, *f* and *g* to simplify the expressions below, and are determined from the reflection plane [*hkl*] and the crystal structure. The angle ϕ is given by eq. (4.3).

$$\cos(\phi) = \text{N.S} = e\cos(\alpha) + f\cos(\beta) + g\cos(\varepsilon) \tag{4.3}$$

Squaring and averaging eq. (4.3) gives eq. (4.4)

$$\left\langle \cos^2(\phi) \right\rangle = e^2 \left\langle \cos^2(\alpha) \right\rangle + f^2 \left\langle \cos^2(\beta) \right\rangle + g^2 \left\langle \cos^2(\varepsilon) \right\rangle + 2ef \left\langle \cos(\alpha)\cos(\beta) \right\rangle$$
$$+2fg \left\langle \cos(\beta)\cos(\varepsilon) \right\rangle + \left\langle 2eg\cos(\alpha)\cos(\varepsilon) \right\rangle \tag{4.4}$$

To determine the average value of $cos^2\varphi$ experimentally, the scattered intensity at a given 2θ was averaged over the azimuthal angle (χ), given by eq. (4.5)

$$\left\langle \cos^2(\phi) \right\rangle = \cos^2(\theta) \left\langle \cos^2(\chi) \right\rangle \tag{4.5}$$

The second term on the right side of eq. (4.5) can be determined from eq. (4.6):

$$\left\langle \cos^2(\chi) \right\rangle = \frac{\int_0^{\pi/2} I(\chi)\cos^2(\chi)\sin(\chi)d\chi}{\int_0^{\pi/2} I(\chi)\sin(\chi)d\chi} \tag{4.6}$$

where *I* is the intensity of the scattered X-rays. In practice, the integrals were replaced by sums as shown in eq. (4.7):

$$\left\langle \cos^2(\chi) \right\rangle = \frac{\sum_0^{\frac{\pi}{2}} I(\chi)\cos^2(\chi)\sin(\chi)}{\sum_0^{\pi 2} I(\chi)\sin(\chi)} \tag{4.7}$$

Eq. (4.4) has a total of six unknowns; hence, without further simplifications, at least five crystal planes would be required to determine the orientation functions in each direction. The orthogonality of the system provides the sixth equation.

$$\cos^2(\alpha) + \cos^2(\beta) + \cos^2(\varepsilon) = 1 \tag{4.8}$$

The angles α, β, ε are evaluated from eq. (4.4). If the pure axial crystal plane reflections can be obtained, then only three planes need to be studied and eq. (4.4). Simplifies, as shown in eq. (4.9):

$$\begin{aligned} \left\langle \cos^2(\phi_{h00}) \right\rangle &= \cos^2(\alpha) \\ \left\langle \cos^2(\phi_{0k0}) \right\rangle &= \cos^2(\beta) \\ \left\langle \cos^2(\phi_{001}) \right\rangle &= \cos^2(\varepsilon) \end{aligned} \tag{4.9}$$

Another simplification can be made for particular crystal structure allowing fewer than five reflection planes to be required. Because PE has an orthorhombic crystal structure that cross-product terms in eq. (4.4) are zero, as shown in eq. (4.10), and only two reflection planes were required for characterization:

$$\left\langle \cos^2(\phi) \right\rangle = e^2 \left\langle \cos^2(\alpha) \right\rangle + f^2 \left\langle \cos^2(\beta) \right\rangle + g^2 \left\langle \cos^2(\varepsilon) \right\rangle \tag{4.10}$$

PE [110] and [200] reflection planes, at 21.4º and 23.7º, respectively, were used for characterization of the crystalline orientation. The values of *e*, *f* and *g* for the [110] reflection plane are 0.554, 0.832, and 0, while those of [200] are 1, 0, and 0, respectively. The orientation of the pure polyethylene films was quantitatively characterized as $\cos^2(\varepsilon)$, where ε is the angle between the stretching direction, **S**, and the polymer chain axis (**Z** axis). The value of $\cos^2(\varepsilon)$ can be between 0 and 1. If the orientation of the chain axis is perpendicular to the stretching direction, then $\cos^2(\varepsilon)$ is 0. If the chain axis is parallel to the stretching direction, then $\cos^2(\varepsilon)$ is 1. When the chain axis is randomly distributed then $\cos^2(\varepsilon)$ is 1/3 [41,42].

Table 4.1 and Figure 4.4 show the orientation of the PE crystallites as a function of draw ratio. It reveals that for unstretched PE crystallites are randomly oriented and by increasing the draw ratio orientation increases. Moreover, 2D WAXS patterns of the various polyethylene films with different draw ratios are shown in Figure 4.5. Patterns show orientation effect: upon stretching rings become arcs in WAXS spectra.

Table 4.1. Orientation of stretched PE as a function of draw ratio

Draw Ratio	**$\cos^2(\varepsilon)$**
1	0.38
2	0.7
3	0.79
4	0.85
6	0.89
7	0.92

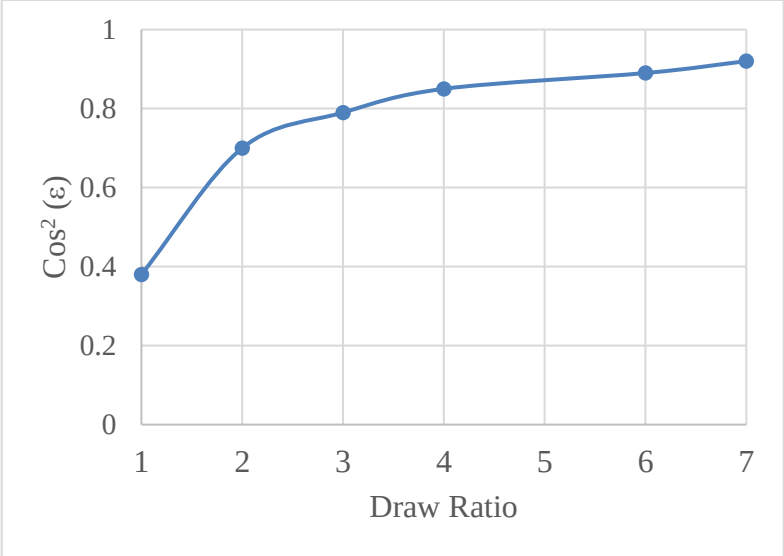

Figure 4.4. Orientation of stretched pure PEs as a function of draw ratio

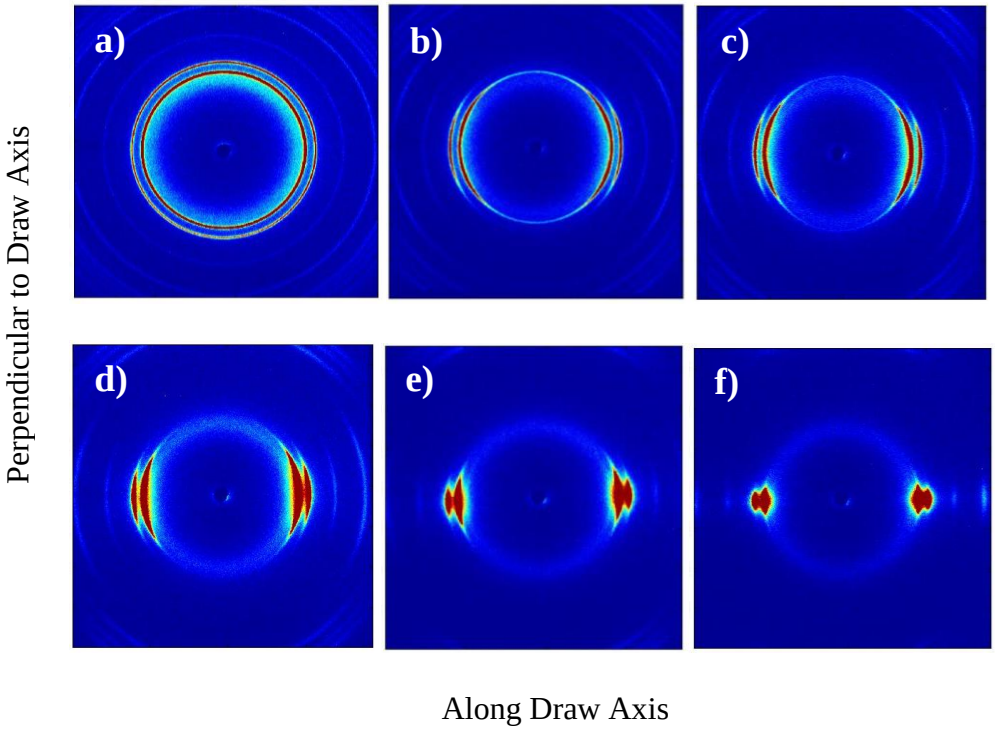

Figure 4.5. WAXS patterns for a) unstretched, b) draw ratio 2, c) draw ratio 3, d) draw ratio 4, e) draw ratio 6 and f) draw ratio 7 for PEs. The stretch direction is horizontal

4.3 Characterization of Alignment of Graphene Flakes Using Laser Scanning Confocal Microscopy (LSCM)

Alignment of graphene flakes within the nanocomposite was studied using Laser Scanning Confocal Microcopy (LSCM). Laser scanning confocal microscopy (LSCM) is a light microscopy technique which creates 3D reconstructions, with up to 300 nm resolution. The focused beam of a laser is scanned over the sample and the reflected intensity is displayed as a function of position to create a digital reflected image of the sample. In conventional microscopes, the light is transmitted through the entire specimen thickness, requiring that the sample is capable of transmitting light, and that bundles do not obscure one another. LSCM circumvents this limitation by utilizing light in the reflected light path, while also blocking any out-of-focus light, creating an image as thin as 300 nm axially, referred to as an optical section. By collecting a series of optical sections along the optical axis (Z-axis), one can generate a 3D reconstruction of a volume within an intact specimen. Scanning a focused laser beam allows the acquisition of digital images with very high resolution since the resolution is determined by the position of the beam rather than the pixel size of the detector.

Confocal microscopy offers several advantages over conventional widefield optical microscopy, including the ability to control depth of field, elimination or reduction of background information away from the focal plane (that leads to image degradation), and the capability to collect serial optical sections from thick specimens. The basic key to the confocal approach is the use of spatial filtering techniques to eliminate out-of-focus light or glare in specimens whose thickness exceeds the immediate plane of focus. There has been a tremendous explosion in the popularity of confocal microscopy in recent years

[43], due in part to the relative ease with which extremely high-quality images can be obtained from specimens prepared for conventional fluorescence microscopy, and the growing number of applications in cell biology that rely on imaging both fixed and living cells and tissues.

4.4 Principles of Confocal Microscopy

The confocal principle in epi-fluorescence laser scanning microscope is diagrammatically presented in Figure 4.6. Coherent light emitted by the laser system (excitation source) passes through a pinhole aperture that is situated in a conjugate plane (confocal) with a scanning point on the specimen and a second pinhole aperture positioned in front of the detector (a photomultiplier tube). As the laser is reflected by a dichromatic mirror and scanned across the specimen in a defined focal plane, secondary fluorescence emitted from points on the specimen (in the same focal plane) pass back through the dichromatic mirror and are focused as a confocal point at the detector pinhole aperture. The significant amount of fluorescence emission that occurs at points above and below the objective focal plane is not confocal with the pinhole (termed Out-of-Focus Light Rays in Figure 4.6 and forms extended Airy disks in the aperture plane.

Because only a small fraction of the out-of-focus fluorescence emission is delivered through the pinhole aperture, most of this extraneous light is not detected by the photomultiplier and does not contribute to the resulting image. The dichromatic mirror, barrier filter, and excitation filter perform similar functions to identical components in a widefield epi-fluorescence microscope. Refocusing the objective in a confocal microscope shifts the excitation and emission points on a specimen to a new plane that becomes confocal with the pinhole apertures of the light source and detector.

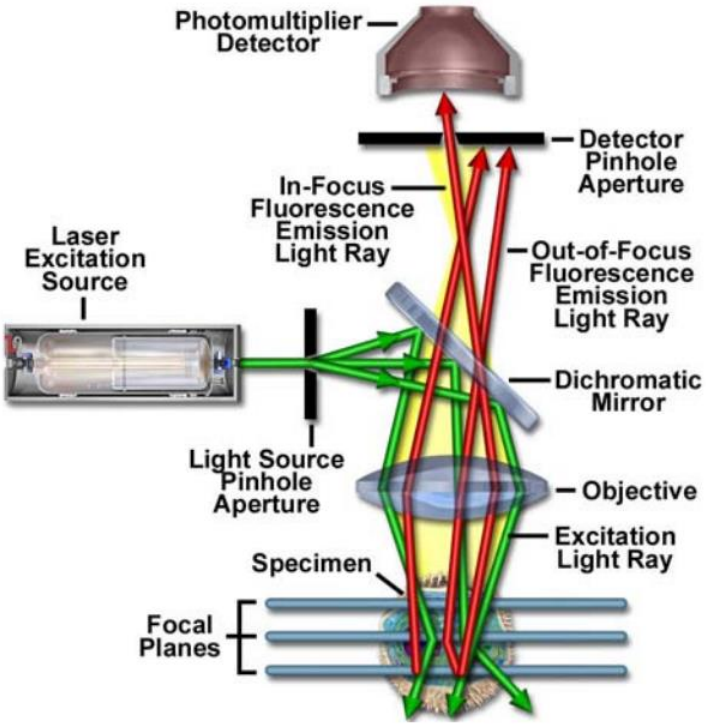

Figure 4.6. Schematic diagram of the optical pathway and principal components in a laser scanning confocal microscope [18]

In traditional widefield epi-fluorescence microscopy, the entire specimen is subjected to intense illumination from an incoherent mercury or xenon arc-discharge lamp, and the resulting image of secondary fluorescence emission can be viewed directly in the eyepieces or projected onto the surface of an electronic array detector or traditional film plane. In contrast to this simple concept, the mechanism of image formation in a confocal microscope is fundamentally different. As discussed above, the confocal fluorescence microscope consists of multiple laser excitation sources, a scan head with optical and electronic components, electronic detectors (usually photomultipliers), and a computer for acquisition, processing, analysis, and display of images. The scan head is at the heart of the confocal system and is responsible for rasterizing the excitation scans, as

well as collecting the photon signals from the specimen that are required to assemble the final image. A typical scan head contains inputs from the external laser sources, fluorescence filter sets and dichromatic mirrors, a galvanometer-based raster scanning mirror system, variable pinhole apertures for generating the confocal image, and photomultiplier tube detectors tuned for different fluorescence wavelengths. Many modern instruments include diffraction gratings or prisms coupled with slits positioned near the photomultipliers to enable spectral imaging (also referred to as emission fingerprinting) followed by linear unmixing of emission profiles in specimens labeled with combinations of fluorescent proteins or fluorophores having overlapping spectra [43–47].

Leica SP8 laser scanning confocal microscope with a 561 nm DPSS laser has been used for imaging in this study. The samples have been imaged with a 63x/1.4 oil immersion objective with the pinhole aperture at 0.2 AU and voxel dimensions of 120 nm x 120 nm x 120 nm and to a depth of 10 µm. Figure 4.7 shows LSCM images of GNPs in unstretched PE/GNP (7 wt%) nanocomposite sample and same composition sample with different stretch ratios. While GNPs are seen to be randomly oriented in Figure 4.7 a, Figures 4.7 b-e clearly show alignment of GNPs along the stretch direction.

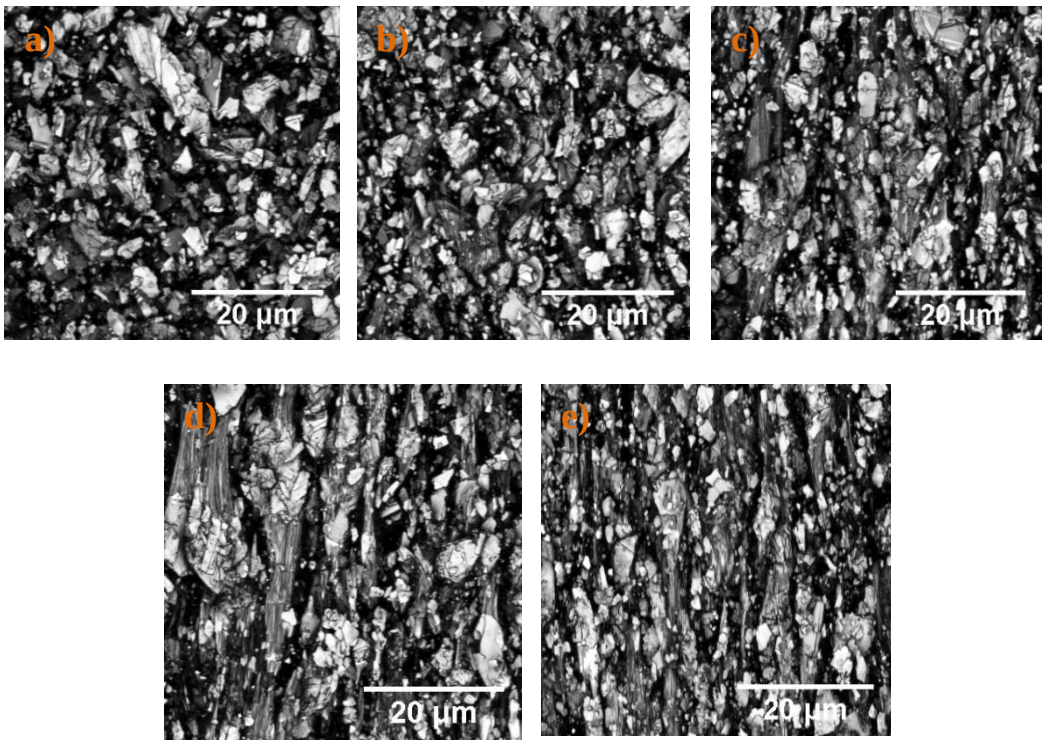

Figure 4.8. LSCM imaging of a PE/GNP sample in a) unstretched and stretched sample with a) draw ratio of 2, c) draw ratio of 3, d) draw ratio of 4 and e) draw ratio of 5

Furthermore, a complete quantitative analysis of GNP alignment within the nanocomposite has been performed by analyzing the images in ImageJ software (version 1.51) to determine the aspect ratio of each GNP in 3D space. The distribution of these ratios is presented in the form of box plot in Figure 4.8.

The aspect ratio is estimated by constructing a bounding box around each GNP flake and extracting the aspect ratio (=length/width) for this box. A bounding box is a rectangular cuboid in 3D, or a rectangle in 2D, containing a single detected object. With this statistical variable, the size of any created objects can be easily determined. For randomly orientated flakes the aspect ratio is expected to be close to 1. For the unstretched sample (σ=1) the measured median value of the ratio is indeed ~1 indicating no alignment

(Figure 4.8). As the sample is stretched, the flakes align themselves along the direction of stretching, increasing length of the bounding box while decreasing the width, resulting in an increase in aspect ratio (=L/W) of the bounding box. Higher aspect ratio is thus a measure of a more aligned orientation of GNP flakes within the nanocomposite. For the stretched samples, it can be seen from that the aspect ratio increases progressively with an increase in draw ratio from σ=2 to σ=5 indicating increasing alignment of GNPs with draw ratio.

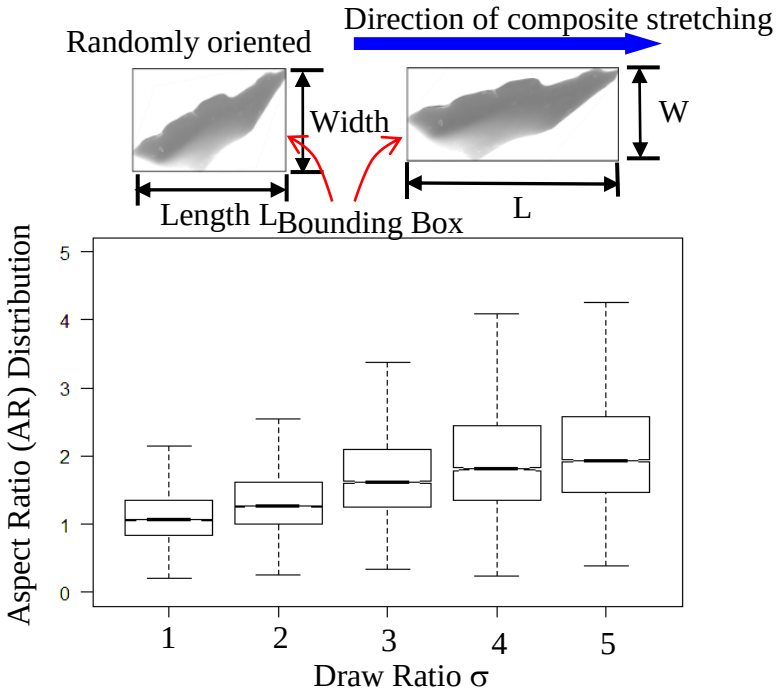

Figure 4.11. Aspect ratio of the GNPs within the PE/GNP (7 wt%) as a function of draw ratio

Chapter 5: Results

This chapter describes the results obtained from this study. Thermal diffusivity has been achieved using the Angstrom method. Specific heat and density of specimens have been obtained using differential scanning calorimeter and pycnometer respectively. Specific heat and density of the specimens have been presented in Table 5.1.

Table 5.1. Specific heat and density of specimens

Sample	Specific Heat [J/gK]	Density [g/cm^3]
Pure Polyethylene	2.18	0.98
PE/GNP (7 wt%)	2.08	1.02
PE/GNP (10 wt%)	2.03	1.04

It has been observed that specific heat of PE/GNP specimen has been slightly decreased which is due to the presence of graphene nanoplatelets. While, density of PE/GNP samples has increased. Calculated thermal conductivity for pure PE, PE/GNP (7wt%) and PE/GNP (10 wt%) for draw ratios between 1 to 5 is presented in Table 5.2.

Table 5.2. Thermal conductivity of pure PE and PE/GNP

Draw Ratio	Thermal Conductivity [W/mK]		
	Pure PE	**PE/GNP (7 wt%)**	**PE/GNP (10 wt%)**
1	0.5	1.0	1.4
2	0.8	2.5	3.3
3	1.5	3.2	4.3
4	2.3	4.1	5.3
5	3.5	5.1	5.9

Moreover, thermal conductivity enhancement as a function of draw ratio is shown in Figure 5.1.

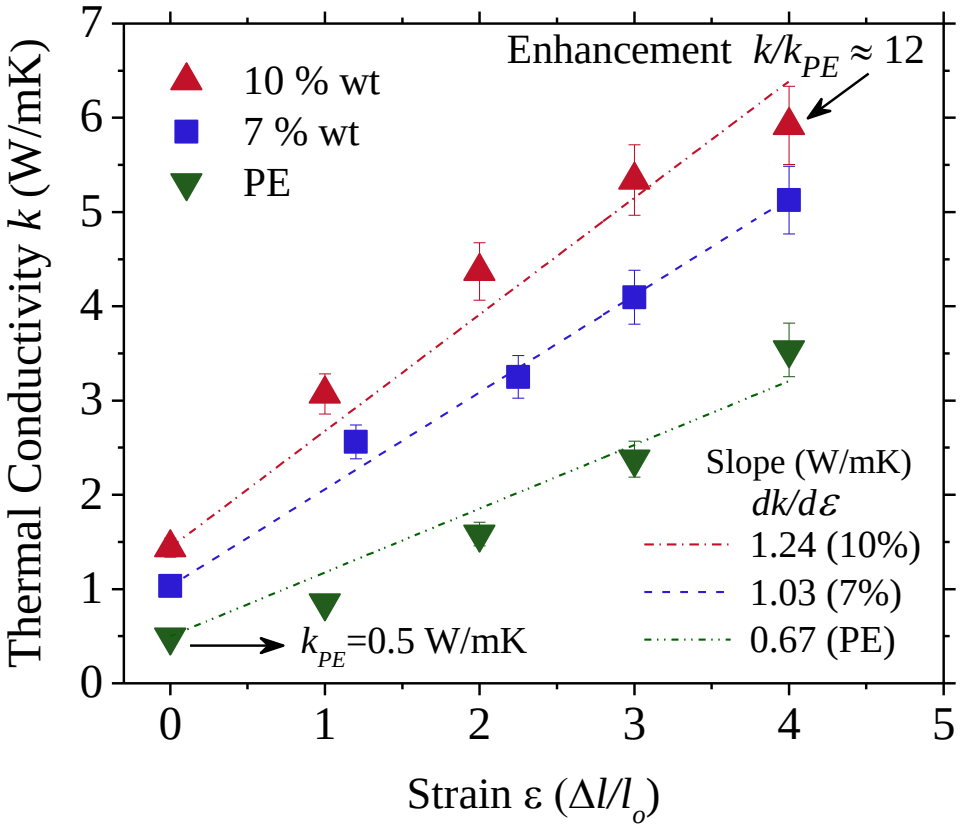

Figure 5.1. Thermal conductivity enhancement of pure PE, PE/GNP (7 wt%) and PE/GNP (10 wt%) as a function of draw ratio

Figure 5.1 shows the first experimental measurements of thermal conductivity of such aligned PE/GNP nanocomposites as a function of draw ratio. PE/GNP nanocomposites were prepared with 7 and 10 wt% GNP (~60 nm thickness, ~5 μm lateral size). Prepared nanocomposites were subjected to permanent stretching (plastic deformation) by different stretch ratios $\sigma (=l/l_0$, where l_0 is the initial sample length and l is the final length after stretching). Notice that $\sigma=1$ corresponds to unstretched sample.

It can be seen in Figure 5.1 that thermal conductivity of the nanocomposite is shifted towards higher values compared to the pure PE case. As the samples are stretched to higher ratios, the increasing alignment of involved components (PE chains and GNPs) with increasing draw ratio leads to a continuous increase in thermal conductivity for the pure PE sample and both PE/GNP nanocomposites. However, while the thermal conductivity of the pure PE sample increased by 3.0 W/mK, upon stretching by 5 times, relative to the unstretched sample, the thermal conductivity of the nanocomposites increased by amount of 4.1 W/mK (7 wt%) and 4.5 W/mK (10 wt%) for the same draw ratio. Thermal conductivity enhancement in pure PE sample is due to alignment of PE chains alone, *k* enhancement in the nanocomposite on the other hand is due to alignment of both PE chains and GNPs. These results provide the first direct and strong evidence that simultaneous alignment of polymer chains and dispersed GNPs can provide high thermal conductivity values.

k-enhancement can also be compared in terms of the slopes of best-fit linear curves for the two samples; $(dk/d\sigma)_{\text{pure-PE}} \approx 0.67$ and $(dk/d\sigma)_{\text{10 wt \% composite}} \approx 1.24$. It should be noted that this ~ 85% increase in slope for the nanocomposite is brought about by an addition of 10 wt% GNP.

Increased effectiveness of aligned GNPs in enhancing thermal conductivity can be further seen by noticing that at $\sigma=1$, the increase in *k* of the nanocomposites relative to pure PE sample is almost 0.5 and 1.0 W/mK for 7 and 10 wt% graphene respectively. This enhancement is through the addition of GNPs flakes which are randomly oriented. At $\sigma=5$, however, the corresponding enhancement is 1.6 and 2.4 W/mK due to 7 and 10 wt% GNP flakes that are more aligned compared to at $\sigma=1$. The presented results thus

provide a new pathway to dramatically enhance the effectiveness of GNP in developing high *k* composite polymeric materials. Finally, it should be noted that the highest thermal conductivity achieved in this work of 5.9 W/mK represents almost 12-fold increase over the *k* of pristine PE (~ 0.5 W/mK). This was achieved at a draw ratio of 5 and by addition of a mere 10 wt% graphene.

Chapter 6: Conclusion and Remarks

In this work, the following four tasks were accomplished to study the effect of alignment on thermal conductivity enhancement of polyethylene-graphene (PE/GNP) nanoplatelets composite materials. First, pure polyethylene and PE/GNP nanocomposites have been synthesized using melt-compounding method. Pure PE has been prepared at 200 ºC with 5 minutes mixing time. PE/GNP nanocomposites with 7 wt% and 10 wt% have been melt-compounded at 200 ºC for 40 minutes. After melt-compounding, compression molding has been performed to prepare the specimens for mechanical stretching. Second, specimens have been stretched using a linear motorized slide. For each of pure PE and PE/GNP (7 and 10 wt%) 5 stretched samples with draw ratios between 2 to 5 have been prepared. Third, several characterization techniques have been performed to study the alignment of polyethylene chains and graphene nanoplatelets. Wide Angle X-ray Spectroscopy (WAXS) and Scanning Electron Microscopy (SEM) have been used for characterization of alignment of polyethylene chains. Moreover, Laser Scanning Confocal Microscopy (LSCM) has been applied to investigate the graphene flakes alignment in PE/GNP nanocomposites. Atomic Force Microscopy (AFM) and SEM used for thickness and lateral size characterization of GNP flakes.

Four, using a created set-up based on the Angstrom method, in-plane thermal conductivity of specimens has been measured. Thermal diffusivity has been extracted from the Angstrom method. Specific heat and density of the specimens have been achieved using Pycnometer and Differential Scanning Calorimeter respectively. Thermal conductivity has been calculated using the below equation:

$$k = \rho s K$$

Where k is thermal conductivity, K is thermal diffusivity, ρ is density and s is specific heat. Effect of molecular alignment on thermal conductivity enhancement of pure PE and PE/GNP (7 and 10 wt%) nanocomposites has been investigated to understand both the effect of graphene flakes alignment and also increase of graphene flakes volume fraction on thermal conductivity (k) enhancement. The obtained results declared the significant impact of alignment on thermal conductivity enhancement. The thermal conductivity of the pure PE sample enhanced by 3.0 W/mK, at draw ratio of 5, in compare to the unstretched specimen. It means the alignment of PE chains led to 7.2 times k enhancement.

Moreover, these results provided the first direct and strong evidence that simultaneous alignment of polymer chains and dispersed GNPs can provide high thermal conductivity values. The thermal conductivity of nanocomposites increased to 5.1 W/mK (7 wt%) and 5.9 W/mK (10 wt%) for the same draw ratio. Thermal conductivity enhancement in pure PE sample is due to alignment of PE chains alone, while k enhancement in the nanocomposite is due to alignment of both PE chains and GNPs.

Furthermore, it has been observed that the highest thermal conductivity achieved in this work of 5.9 W/mK represents almost 12-fold increase over the k of pristine PE (~ 0.5 W/mK). This was achieved at a draw ratio of 5 and by addition of 10 wt% GNP flakes.

References

[1] E. Kolasinska, P. Kolasinski, A review on electroactive polymers for waste heat recovery, Materials (Basel). 9 (2016) 1–15. doi:10.3390/ma9060485.

[2] X. Chen, Y. Su, D. Reay, S. Riffat, Recent research developments in polymer heat exchangers - A review, Renew. Sustain. Energy Rev. 60 (2016) 1367–1386. doi:10.1016/j.rser.2016.03.024.

[3] C. Dreiser, Polymer Film Heat Exchanger for Seawater Desalination : Prevention and Cleaning of Fouling Deposits, 2013 (2013) 296–301.

[4] W. Liu, J. Davidson, S. Mantell, Thermal analysis of polymer heat exchangers for solar water heating: acasestudy., Sol Energy Eng Trans ASME. 122 (2000) 84–91.

[5] S. Mallik, N. Ekere, C. Best, R. Bhatti, Investigation of thermal management materials for automotive electronic control units, Appl. Therm. Eng. 31 (2011) 355–362. doi:10.1016/j.applthermaleng.2010.09.023.

[6] P. Procter, J. Solc, Improved Thermal Conductivity in Microelectronic Encapsulants, IEEE Trans. Components, Hybrids, Manuf. Technol. 14 (1991) 708–713. doi:10.1109/33.105121.

[7] X. Lu, G. Xu, Thermally Conductive Polymer Composites for Electronic Packaging, J. Appl. Polym. Sci. 65 (1997) 2733–2738. doi:10.1002/(SICI)1097-4628(19970926)65:13%3C2733::AID-APP15%3E3.0.CO;2-Y.

[8] J. Garg, Relative effect of edge versus basal plane functionalization on graphene/polymer interfacial thermal conductance - Role of in-plane phonons, Appl. Phys. Lett. 110 (2017) 93112. doi:10.1063/1.4977433.

[9] D.M. Bigg, G.H. Stickford, S.G. Talbert, Applications of polymeric materials for condensing heat exchangers, Polym. Eng. Sci. 29 (1989) 1111–1116. doi:10.1002/pen.760291607.

[10] P. Luckow, A. Bar-cohen, P. Rodgers, J. Cevallos, Efficient Polymers for Seawater Heat Exchangers rnationa l Energy, Second Int. Energy 2030 Conf. 132 (2008) 138–141. doi:10.1115/1.4001568.

[11] J. Yu, B. Sundqvist, B. Tonpheng, O. Andersson, Thermal conductivity of highly crystallized polyethylene, Polym. (United Kingdom). 55 (2014) 195–200. doi:10.1016/j.polymer.2013.12.001.

[12] G. Fugallo, A. Cepellotti, L. Paulatto, M. Lazzeri, N. Marzari, F. Mauri, Thermal conductivity of graphene and graphite: Collective excitations and mean free paths, Nano Lett. 14 (2014) 6109–6114. doi:10.1021/nl502059f.

[13] S. Ghosh, W. Bao, D.L. Nika, S. Subrina, E.P. Pokatilov, C.N. Lau, A. a Balandin, Dimensional crossover of thermal transport in few-layer graphene., Nat. Mater. 9 (2010) 555–558. doi:10.1038/nmat2753.

[14] A.A. Balandin, S. Ghosh, W. Bao, I. Calizo, D. Teweldebrhan, F. Miao, C.N. Lau, Superior thermal conductivity of single-layer graphene, Nano Lett. 8 (2008) 902–907. doi:10.1021/nl0731872.

[15] A. Brown, X-ray diffraction studies of the stretching and relaxing of polyethylene, J. Appl. Phys. 20 (1949) 552–558. doi:10.1063/1.1698424.

[16] S.L. Aggarwal, G.P. Tilley, O.J. Sweeting, Changes in orientation of crystallites during stretching and relaxation of polyethylene films, J. Polym. Sci. 51 (1961) 551–568. doi:10.1002/pol.1961.1205115612.

[17] G. Vancso, D. Snétivy, I. Tomka, Structural changes during polystyrene orientation: A study of optical birefringence and wide angle X-ray scattering, J. Appl. Polym. Sci. 42 (1991) 1351–1359. doi:10.1002/app.1991.070420518.

[18] <www.segerfrojd.com> Segerfrojd, A. B. Polypropylene heat exchanger, Stretch-modulated carbon nanotube alignment in ferroelectric polymer composites: Characterization of the orientation state and its influence on the dielectric properties, J. Phys. Chem. C. 115 (2011) 20011–20017. doi:10.1021/jp205444x.

[19] <www.segerfrojd.com> Segerfrojd, A. B. Polypropylene heat exchanger, Alignment of carbon nanotubes in a polymer matrix by mechanical stretching, Appl. Phys. Lett. 73 (1998) 1197–1199. doi:10.1063/1.122125.

[20] <www.segerfrojd.com> Segerfrojd, A. B. Polypropylene heat exchanger, Polymers with aligned carbon nanotubes: Active composite materials, Polymer (Guildf). 49 (2008) 3841–3854. doi:10.1016/j.polymer.2008.05.005.

[21] B. Nysten, P. Gonry, J.P. Issi, Intra- and interchain thermal conduction in polymers, Synth. Met. 69 (1995) 67–68.

[22] A. Henry, G. Chen, High thermal conductivity of single polyethylene chains using molecular dynamics simulations, Phys. Rev. Lett. 101 (2008) 1–4. doi:10.1103/PhysRevLett.101.235502.

[23] B. Poulaert, J.C. Chielenst, C. Vandenhendej, J.P. Issi, R. Legras, Thermal conductivity of highly oriented polyethylene fibres, Polym. Commun. 31 (1990) 148–151.

[24] D. Mergenthaler, M. Pietralla, S. Roy, H. Kilian, Thermal conductivity in ultraoriented polyethylene, Macromolecules. 25 (1992) 3500–3502. doi:10.1021/ma00039a030.

[25] S. Shen, A. Henry, J. Tong, R. Zheng, G. Chen, Polyethylene nanofibres with very high thermal conductivities., Nat. Nanotechnol. 5 (2010) 251–5. doi:10.1038/nnano.2010.27.

[26] J. Loomis, H. Ghasemi, X. Huang, N. Thoppey, J. Wang, J.K. Tong, Y. Xu, X. Li, C.-T. Lin, G. Chen, Continuous fabrication platform for highly aligned polymer films, Technology. 2 (2014) 1–11. doi:10.1142/S2339547814500216.

[27] H. Huang, C. Liu, Y. Wu, S. Fan, Aligned carbon nanotube composite films for thermal management, Adv. Mater. 17 (2005) 1652–1656. doi:10.1002/adma.200500467.

[28] A.M. Marconnet, N. Yamamoto, M. a. Panzer, B.L. Wardle, K.E. Goodson, Thermal Conduction in Aligned Carbon Nanotube- Polymer Nanocomposites

with High Packing Density, ACS Nano. 5 (2011) 4818–4825. doi:10.1021/nn200847u.

[29] D. Kumlutaş, I.H. Tavman, M. Turhan Çoban, Thermal conductivity of particle filled polyethylene composite materials, Compos. Sci. Technol. 63 (2003) 113–117. doi:10.1016/S0266-3538(02)00194-X.

[30] C.M. Ye, B.Q. Shentu, Z.X. Weng, Thermal conductivity of high density polyethylene filled with graphite, J. Appl. Polym. Sci. 101 (2006) 3806–3810. doi:10.1002/app.24044.

[31] I.H. Tavman, Thermal and mechanical properties of aluminum powder-filled high-density polyethylene composites, J. Appl. Polym. Sci. 62 (1996) 2161–2167. doi:10.1002/(SICI)1097-4628(19961219)62:12<2161::AID-APP19>3.3.CO;2-A.

[32] R. Haggenmueller, C. Guthy, J.R. Lukes, J.E. Fischer, K.I. Winey, Single wall carbon nanotube/polyethylene nanocomposites: Thermal and electrical conductivity, Macromolecules. 40 (2007) 2417–2421. doi:10.1021/ma0615046.

[33] E. Pop, V. Varshney, A. Roy, Thermal properties of graphene: Fundamentals and applications, Mrs Bull. 1273 (2012) 1–28. doi:10.1557/mrs.2012.203.

[34] A.A. Balandin, Thermal properties of graphene and nanostructured carbon materials., Nat. Mater. 10 (2011) 569. doi:10.1038/nmat3064.

[35] M.T. Pettes, I. Jo, Z. Yao, L. Shi, Influence of polymeric residue on the thermal conductivity of suspended bilayer graphene, Nano Lett. 11 (2011) 1195–1200. doi:10.1021/nl104156y.

[36] J. Haskins, A. Kinaci, C. Sevik, H. Sevinçli, G. Cuniberti, T. Çağin, Control of thermal and electronic transport in defect-engineered graphene nanoribbons, ACS Nano. 5 (2011) 3779–3787. doi:10.1021/nn200114p.

[37] J.H. Seol, I. Jo, A.L. Moore, L. Lindsay, Z.H. Aitken, M.T. Pettes, X. Li, Z. Yao, R. Huang, D. Broido, N. Mingo, R.S. Ruoff, L. Shi, Two-dimensional phonon

transport in supported graphene., Science. 328 (2010) 213–6. doi:10.1126/science.1184014.

[38] Z. Aksamija, I. Knezevic, Lattice thermal conductivity of graphene nanoribbons: Anisotropy and edge roughness scattering, Appl. Phys. Lett. 98 (2011) 3–5. doi:10.1063/1.3569721.

[39] K.F. Mak, C.H. Lui, T.F. Heinz, Measurement of the thermal conductance of the graphene/ SiO2 interface, Appl. Phys. Lett. 97 (2010) 2010–2013. doi:10.1063/1.3511537.

[40] I. Childres, L. Jauregui, W. Park, H. Cao, Y. Chen, Raman Spectroscopy of Graphene and Related Materials, New Dev. Phot. Mater. Res. (2013) 1–20. doi:10.1016/B978-0-444-53175-9.00016-7.

[41] W.B. Genetti, R.J. Lamirand, B.P. Grady, Wide-angle X-ray scattering study of crystalline orientation in reticulate-doped polymer composites, J. Appl. Polym. Sci. 70 (1998) 1785–1794. doi:10.1002/(SICI)1097-4628(19981128)70:9<1785::AID-APP17>3.0.CO;2-8.

[42] C.M. Burba, R. Frech, B. Grady, Stretched PEO-LiCF3SO3 films: Polarized IR spectroscopy and X-ray diffraction, Electrochim. Acta. 53 (2007) 1548–1555. doi:10.1016/j.electacta.2007.04.035.

[43] S.W. Paddock, Microscopy Edited by, Methods. 122 (1949) 446. doi:10.1385/159259722X.

[44] T. Wilson, A.R. Carlini, Three dimensional imaging in confocal imaging systems with finite sized detectors, J. Microsc. 149 (1988) 51–66. doi:10.1111/j.1365-2818.1988.tb04561.x.

[45] L. Microscopy, M. Science, Q. Mary, Quantitative fluorescence resonance energy transfer (FRET) measurement with acceptor photobleaching and spectral unmixing, 215 (2004) 162–173.

[46] M.E. Dickinson, G. Bearman, S. Tille, R. Lansford, S.E. Fraser, Multi-spectral imaging and linear unmixing add a whole new dimension to laser scanning

flourescence microscopy, Bioimaging. 31 (2001) 1272–1278. doi:citeulike-article-id:2534922.

[47] G. Bearman, R. Lansford, S. Fraser, Resolution of multiple green fluorescent protein color variants and dyes using two-photon microscopy and imaging spectroscopy, J. Biomed. Opt. 6 (2001) 311–318. doi:10.1117/1.1383780.